# Nanoscale

Accepted Manuscript


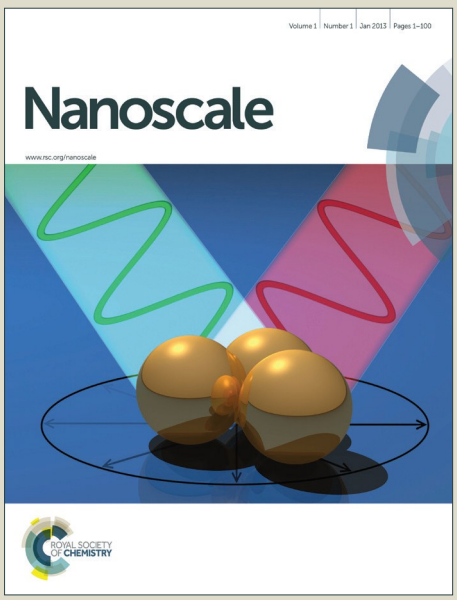





ROYAL SOCIETY OF CHEMISTRY

www.rsc.org/nanoscale

Nanoscale

ARTICLE

# Cobalt sulfide/N, S Co-doped porous carbon core-shell nanocomposites as superior bifunctional electrocatalysts for oxygen reduction and evolution reactions

Received 00th January 20xx,
Accepted 00th January 20xx

DOI: 10.1039/x0xx00000x

www.rsc.org/

Binling Chen,[a] Rong Li,[b] Guiping Ma,[a,c] Xinglong Gou,[b] Yanqiu Zhu,[a] and Yongde Xia*[a]

Exploring highly-efficient and low-cost bifunctional electrocatalysts for both oxygen reduction reaction (ORR) and oxygen evolution reactions (OER) in the renewable energy area has gained its momentum but still remains a significant challeng. Here we represent a simple but efficient way that utilizes ZIF-67 as the precursor and template for the one-step generation of homogeneous dispersed cobalt sulfide/N,S-codoped porous carbon nanocomposites as high-performanc electrocatalysts. Due to the favourable molecular-like structural features and uniform dispersed active sites in the precursor, the resulting nanocomposites featured with unique core-shell structure, high porosity, homogeneous dispersion active components together with N and S-doping effect, not only show excellent electrocatalytic activity towards ORR with the high onset potential (around -0.04 V vs -0.02 V for benchmark Pt/C catalyst) and four-electron pathway, and OER with a small overpotential of 0.47 V for 10 mA $cm^{-2}$ current density, but also exhibit superior stability (92%) to commercial Pt/C catalyst (74%) in ORR and promising OER stability (80%) with good methanol tolerance. Our findings suggest that the transition metal sulfide-porous carbon nanocomposites derived from the one-step simultaneously sulfurization and carbonization of zeolitic imidazolate frameworks are excellent alternative bifuncitonal electrocatalysts towards ORR and OER in the next generation of energy storage and conversion technologies.

With the depletion of hydrocarbon-based energy resources and the increasing global energy demands, it is imperative to develop green and sustainable energy storage and conversion technologies as alternatives to currently widely used fossil fuels.[1-3] Electrocatalytic oxygen reduction reaction (ORR) and oxygen evolution reaction (OER) play key roles in several important next-generation energy storage and conversion technologies, such as fuel cells, metal-air batteries and water splitting.[4-13] Hitherto, most efficient electrocatalysts for ORR/OER contain precious metals including Pt or Ir; however, due to the prohibitive cost, poor stability of precious metals, the sluggish kinetics for ORR and the large polarisation, it is highly desirable to discover highly efficient and low-cost earth-abundant non-precious electroactive materials that can rival the performances of precious metal-based catalysts.[14-17]

Many efforts have, therefore, been devoted to transition metal oxides/sulfides based materials, as many transition metals like cobalt, manganese have been widely considered to be electrochemical active for ORR and OER. Particularly, cobalt sulfides ($Co_xS_y$) with different phases have been previously investigated as ORR and OER electrode catalysts and exhibited attractive electrocatalytic performance among different non-precious and late transition metal chalcogenides.[18-23] For instance, $CoS_2$ is a good electrocatalyst for ORR and OER; $Co_3S_4$ has excellent performance for ORR[25, 26] and OER;[26] while $Co_{1-x}S$ is a promising electrocatalyst for ORR[18, 26] and OER; $Co_9S_8$ is a good catalyst for ORR.[21] However, the complicated preparation procedures coupled with the low electrical conductivities of cobalt sulfides usually result in the catalytic durability unsatisfactory. As alternatives, transition metal oxide/sulfide-carbon composites have been considered as promising electrocatalysts for ORR/OER since they hold a reasonable balance between catalytic activity, cost, and durability.[27] In particular, heteroatom (e.g., N, S, B, or P) doped carbon based materials have emerged and attracted great attention because heteroatom can tune the electronic and geometric properties of carbon, offering more active sites and enhancing the interaction between carbon structure and active sites.[27-30] Remarkably, the combination of transition metal metal oxide/sulfide with heteroatom-doped carbon can achieve high catalytic activity and improve durability because of the synergetic effect.[27]

Metal organic frameworks (MOFs, including Zeolitic Imidazolate Frameworks (ZIFs)), a class of nanoporous materials assembled from metal ions and organic ligands,[31-33]

[a] College of Engineering, Mathematics and Physical Sciences, University of Exeter, Exeter EX4 4QF, United Kingdom.
[b] Chemical Synthesis and Pollution Control Key Laboratory of Sichuan Province, College of Chemistry and Chemical Engineering, China West Normal University, Nanchong 637000, P R China.
[c] State Key Laboratory of Chemical Resource Engineering, Beijing Laboratory of Biomedical Materials, Beijing University of Chemical Technology, Beijing 100029, P R China.
* Corresponding author. E-mail address: y.xia@exeter.ac.uk (Y. Xia) Electronic Supplementary Information (ESI) available:
See DOI: 10.1039/x0xx00000x

exhibit tuneable structures, versatile functionalities and fascinating properties. Owing to the molecular-like organic-inorganic crystal structure of MOFs, thermal treatment the parental MOFs can result in the formation of metal or metal oxide nanoparticles homogeneously dispersed within the nanoporous carbon matrices which frequently exhibit excellent electrochemical properties.[34-39] Therefore, MOFs have emerged as excellent precursors or sacrificial templates for the preparation of porous carbon based nanocomposites, which offer a new approach to improve the catalytic activity and overcome the intrinsic limitations of the existing transition metal/metal oxide electrocatalysts.[34, 35, 37-39] Metal sulfides derived from MOFs were recent reported;[40, 41] however, to the best our knowledge, carbon-based metal sulfide composites derived from MOFs as highly efficient electrocatalysts for ORR/OER are rarely reported previously.

Herein, for the first time, we report the successful synthesis of atomically homogeneous dispersed cobalt sulfide/N,S-codoped porous carbon nanocomposites by a facile one-step sulfurization and carbonization of ZIF-67 simultaneously. ZIF-67 was chosen as a model precursor owing to its abundant Co–N moieties, rich organic resources and unique dodecahedral morphology.[33] Possessing unique core-shell structure, high porosity, homogeneous dispersion active components together with N and S-doping effect, the resulting composites exhibit excellent ORR and OER activities, superior durability, a four-electron pathway and high methanol tolerance in alkaline media, which outperformed the traditional Pt/C electrocatalyst. This may pave the way to further develop novel highly-efficient and low-cost composite electrocatalysts for the next generation of energy storage and conversion applications.

## Experimental

### Materials synthesis

ZIF-67 was synthesized from cobalt nitrate hexahydrate and 2-methylimidazole in water, following a modified procedure.[42] The porous nanocomposites were prepared by a one-step direct carbonization and sulfurization process in the presence of hydrogen sulfide. In a typical synthesis, an alumina boat loaded with 0.25 g of dried ZIF-67 was placed in a flow-through quartz tube sitting in the centre of a tube furnace. The furnace was firstly heated to the target temperature (typically 600 – 1000 °C) with ramp rate 10 $^{o}$C/min under pure argon atmosphere; when the furnace temperature reached the target temperatures, a 20 mL/min of hydrogen sulfide was then introduced in and maintained at the target temperature for 1 hour. The gas flow was then switched to argon only during the furnace cooled down to room temperature. The final product was collected from the quartz tube and labelled as $Co_xS_y$@C-z, where z stands for the sulfurization and carbonization temperature. Therefore the sample obtained from sulfurization temperature of 600, 800 and 1000 $^{o}$C was labelled as $Co_xS_y$@C-600, $Co_xS_y$@C-800 and $Co_xS_y$@C-1000 respectively.

### Materials characterization

X-ray diffraction (XRD) patterns were recorded with a Cu Kα radiation (40 kV-40 mA) at a step time of 1 s and a step size of 0.02$^{o}$. The Raman spectra of the samples were recorded in the backscattering arrangement, using a 532 nm laser excitation under laser power of 6 mW. Thermogravimetric analysis (TGA)/differential thermal analysis (DTA) was performed on a TA SDT Q600 instrument from the room temperature to 800 °C with a heating rate of 10 $^{o}$C min$^{-1}$ under a continuous air flow of 100 mL min$^{-1}$. A Hiden QGA gas analysis mass spectrometer (MS) was coupled with the Q600 instrument to monitor and detect the gaseous compositions in the exhaust emission. Scanning electron microscopy (SEM) and Energy-dispersive X-ray spectroscopy (EDX) analyses were carried out on a Philips XL-30 machine in a high vacuum mode at an acceleration voltage of 20 kV. Samples were mounted using a conductive carbon double-sided sticky tape, then sputtered with a thin Au coating to reduce the effects of charging. Transmission electron microscopy (TEM) images were obtained on a JOEL 2100 at an acceleration voltage of 200 kV. The powder samples were first dispersed in absolute ethanol under moderate sonication, then pipetted onto a holey carbon Cu grid to obtain TEM specimens. $N_2$ gas sorptions were carried out on a Quantachrome Autosorb-iQ gas sorptometer via the conventional volumetric technique. Before gas analysis, the sample was evacuated for 3 hours at 200 °C under vacuum. The textural properties were determined via $N_2$ sorption at 196 °C. The surface area was calculated using the Brunauer-Emmett-Teller (BET) method based on adsorption data in the partial pressure (*P*/*P*o) range of 0.02-0.22. The total pore volume was determined from the amount of nitrogen adsorbed at *P*/*P*o of *ca*. 0.99. X-ray photoelectron spectroscopy (XPS) was performed using a Kratos AXIS ULTRA spectrometer with a mono-chromated Al KR X-ray source (1486.6 eV) operated at 10 mA emission current and 15 kV anode potential. The analysis chamber pressure was better than 1.3×10$^{-12}$ bar. The take-off angle for the photoelectron analyzer was 90$^{o}$, and the acceptance angle was 30$^{o}$ (in magnetic lens modes).

### Electrocatalytic measurements

The electrocatalytic performance of the catalysts was evaluated by cyclic voltammograms (CV), linear sweep voltammograms (LSV) and chronoamperometry in a three electrode electrochemical cell which was connected to a computer controlled potentiostat CHI 760D, coupled with a rotating disk electrode (RDE) system. A platinum wire and a Ag/AgCl/KCl (saturated solution) were used as the counter electrode and the reference electrode, respectively. A 3 mm in diameter bare glassy carbon electrode (GCE) or modified GCE with the studied material was used as the working electrode. Prior to use, GCE was hand-polished with chamois leather containing 0.05 µm alumina slurry to obtain a mirror-like surface, washed with ethanol and distilled water by sonication for 5 min and allowed to dry. The modified GCE was prepared by casting a 5 µL aliquot of the catalyst ink, which was obtained by ultrasonically dispersing 1 mg of the catalyst into 0.5 mL 0.05 wt% in alcohol Nafion solution, onto the fr

surface of the pretreated GCE electrode and dried naturally to form a uniform thin film. The loading amount of each catalyst was kept to be 141.5 μg $cm^{-2}$. The experiments were carried

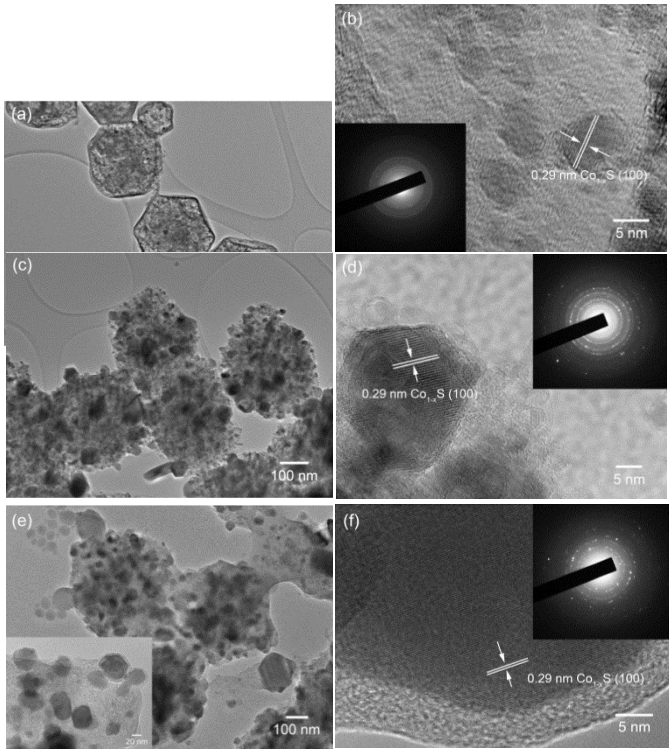


**Fig. 1 TEM images of (a-b) $Co_xS_y$@C-600; (c-d) $Co_xS_y$@C-800 and (e-f) $Co_xS_y$@C-1000. Inset in (b), (d) and (f) is SAED patterns for corresponding sample.**

out at room temperature in 0.1 M KOH solution, which was purged with high purity nitrogen or oxygen with a flow rate of 20 mL $min^{-1}$ for at least 30 min prior to each measurement. All potentials were measured and reported *vs* the Ag/AgCl reference electrode.

## Results and discussion

The structure and morphology of cobalt sulfide/N,S-codoped porous carbon composites samples are firstly investigated by transmission electron microscopy (TEM). The parental ZIF-67 precursor exhibits a typical rhombic dodecahedron with an average particle size of 350 nm (Fig. S1†).[42] After sulfurization and carbonization process in hydrogen sulfide atmosphere at high temperatures, as presented in Fig. 1, the resulting cobalt sulfide/N,S-codoped porous carbon composites maintain the rhombic dodecahedron particles with a smaller size of 250 nm due to the shrinkage during the annealing process, and the particles tend to agglomerate and form larger particles at higher temperatures. Generally, all the composites are composed of numerous cobalt sulfides nanoparticles and continuous carbon networks, in which the cobalt sulfides nanoparticles are homogeneously embedded into the carbon matrix, with lattice fringes of ~0.29 nm. The selected area electron diffraction (SAED) patterns shown in Inset of Fig. 1b, d and f, clearly suggest that the bright scattered dots contribute from the crystalline cobalt sulfide nanoparticles while the dimmed diffraction rings are from the amorphous porous carbon matrix.[18] In addition, the particle sizes for cobalt sulfide grow from 5 to 50 nm with the increase of annealing temperature from 600 °C to 1000 °C, and the corresponding intensity of SAED patterns are also enhanced due to the increased annealing temperature resulting in the improved crystallization of cobalt sulfide particles. In particular, sample $Co_xS_y$@C-600 still maintains the original rhombic dodecahedron of the ZIF-67 precursor. Small cobalt sulfide nanoparticles (5 nm) are homogeneously dispersed into the carbon matrix. The surface of the sample $Co_xS_y$@C-600 is smooth (see the SEM in Fig. S2a†). While the sample $Co_xS_y$@C-800 shows slightly changed morphology because of the growing bigger cobalt sulfide crystals and its surfaces turn to rough (see Fig. S2b†), which is consistent with TEM results (Fig. 1c). Furthermore, high resolution TEM (Fig. 1d) indicates that onion-like carbon, which is formed due to the catalytic effect of metallic cobalt during the graphitization stage,[36, 38] together with bigger cobalt sulfide particles (20 nm) can be observed. However, the sample $Co_xS_y$@C-1000 exhibit damaged or distorted rhombic dodecahedron morphology due to the higher annealing temperature, and cobalt sulfide crystals grow up to 50 nm (shown in Fig. 1e and Fig. S2c†). Interestingly, crystalline cobalt sulfide core and carbon shell structure is formed in the sample $Co_xS_y$@C-1000 (shown in Fig. 1e and f). This core-shell structure is also confirmed by using linear EDX analysis in STEM measurements (shown in Fig. S3†). The thickness of carbon shell is about 5 nm, which has tightly wrapped the cobalt sulfide crystals. Actually, core-shell structure has been proven to be beneficial to the improvement of electrocatalytic activities towards ORR and OER, where the core offers the catalytic active sites while the shell will provide facile electron transfer pathways and mass transport channels for the active cores due to the porous structures of carbon shell.[27, 43]

Moreover, SEM combined with elemental mapping technique was used to ascertain the distribution of cobalt sulfide nanoparticles in the composite samples. As shown in Fig. S4†, element Co, S and C exhibit similar elemental mapping patterns to their selected area of SEM image, indicating the uniform dispersion of cobalt sulfide nanoparticles in the carbon matrix of sample $Co_xS_y$@C-1000. In addition, N is also observed in the elemental mapping although N content is much less than that of C, possibly due to the high volatility of N species at high annealing temperature.

The crystal structures of the as-synthesized $Co_xS_y$@C composites were further characterized by XRD (shown in Fig. 2a). Different from the Sodalite structure of ZIF-67 precursor (Fig. S1b†), the as-prepared composites show a broad XRD peak centred at 2θ of around 25°, representing the (002) diffraction of carbon.[44] Moreover, the XRD patterns of the composites indicate that they contain mainly $Co_{1-x}S$ (ICDD PDF #42-0826) with the hexagonal structure in P63/mmc space group (no. 194).[18] In addition, in sample $Co_xS_y$@C-1000, XRD peaks originated from $Co_3S_4$ (ICDD PDF #02-0825) can also

observed, indicating the phase transition of cobalt sulfide crystals occurs at higher annealing temperature (1000 °C). Clearly, high sulfurization and carbonization temperature results in highly crystalized cobalt sulfide dispersed in carbon

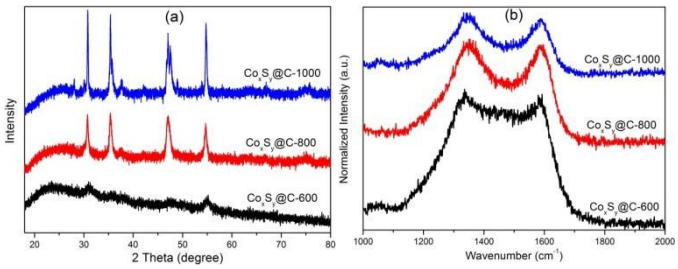


**Fig. 2 (a) XRD patterns and (b) Raman spectra of the as-synthesized $Co_xS_y$@C composites.**

matrix. The XRD results are consistent with the lattice fringes of the $Co_{1-x}S$ nanocrystals (Fig. 1b, d and f) and their electron diffraction patterns (the inset in Fig. 1d and Fig. 1f). Although it is ideal to achieve phase pure cobalt sulfide materials via control over the sulfurization temperature, it is actually difficult to achieve this using the proposed experimental procedure, which is consistent with the recent reports,[45, 46] where the authors used sulfur for the sulfurization of ZIF-67 under different temperatures and the formation of the as-synthesized composites is complicated during the sulfurization and carbonization procedure. The XRD results clearly showed that with the increase of sulfurization temperatures, the XRD peaks for cobalt sulfide (mainly $Co_{1-x}S$ phase) became more intense and sharper, accompanied with the appearing of $Co_3S_4$, indicating the growth of crystallites and crystallinity improvement of cobalt sulfide. And both $Co_{1-x}S$ and $Co_3S_4$ are regarded as good electrocatalysts for ORR and OER.[18, 26] It is, however, worthy to understand the formation mechanism of cobalt sulfide in this relatively complicated system.

Raman spectroscopy is a powerful technique to investigate carbonaceous materials. As shown in Fig. 2b, all the composites clearly exhibit G band and D band in the Raman spectra, due to the bond stretching of all pairs of $sp^2$ atoms in both rings and chains and the breathing modes of $sp^2$ atoms in rings, respectively.[47, 48] The G band at around 1590 $cm^{-1}$ supports the presence of some nanocrystalline carbon and a high content of $sp^2$-hybridized carbon atoms caused by the carbonization of the samples. The D band at around 1340 $cm^{-1}$ is an indication of less disordered carbon. The appearance of both G band and D band in sample $Co_xS_y$@C-600, $Co_xS_y$@C-800, $Co_xS_y$@C-1000, suggests the formation of abundant defects and amorphous carbon in the composites during the sulfurization and carbonization process.

X-ray photoelectron spectroscopy (XPS) analysis was utilised to ascertain the structures of as-synthesized composites owing to the fairly complex phase diagram of cobalt sulphide.[49] Element survey by XPS (Fig. 3a) clearly suggests the presence of Co, S, C, N, and O in all the composites.[27, 50] The spectrum of Co 2p (shown in Fig. 3b) for sample obtained at sulfurization temperature of 600 °C ($Co_xS_y$@C-600) exhibits two spin-orbit doublets at 781.2 and 796.9 eV, implying the existence of $Co^{2+}$ oxidation state. However, except the spin-orbit doublets for $Co^{2+}$ oxidation state, another doublets at 778.4 and 793.5 eV, which indicate the existence of $Co^{3+}$ oxidation state,[51, 52] can be found in the sample $Co_xS_y$@C-800 and $Co_xS_y$@C-1000, suggesting that a mixed $Co^{2+}$ and $Co^{3+}$ oxidation states are formed in these two samples.[51-53] In S 2p spectrum (shown in Fig. 3c), the first two peaks located at 161.4 and 162.5 eV were due to the spin–orbit coupling in metal sulfide,[53, 54] while S 2p peak at 163.5 eV suggested the existence of covalent S-C bonds in the as-synthesized composites[55, 56] indicating that S has been covalently inserted in N-doped porous carbon.[43] No peaks at around 164.5 eV corresponds to polysulfides ($S_n^{2-}$) can be found in all samples,[57-59] and the peaks at 168.5 and 169.5 eV in S 2p spectrum indicate that inconsequential amount of $Co_xS_y$ compounds were also formed during the thermal treatment process.[60, 61] Moreover, the main peaks for N 1s spectra (shown in Fig. 3d) can be deconvoluted into four different types of nitrogen species: pyridinic-N (397.8 eV), Co-N (399.1 eV), pyrrolic-N (400.1 eV), and graphitic-N (401.8 eV), respectively.[39] The N species is widely considered to play an important role in the ORR and OER processes,[62, 63] where pyridinic N could improve the onset potential and graphitic N determined the limiting current for ORR.[27, 50] It is clear that high temperature results in low N content remaining in the samples, maybe due to the high volatility of N species under high temperature sulfurization process. From XPS results, the nitrogen doping level in sample $Co_xS_y$@C-1000 and $Co_xS_y$@C-800 is relatively low (2.51% and 3.64% respectively), sample $Co_xS_y$@C-600 possesses relatively high nitrogen content, and all the samples contain different level of sulfur content. However, it is not easy to evaluate the contribution of S doping to the catalytic activity separately in these complicated system. The C 1s spectrum of the composites (Fig. S5a†) exhibits a main peak at 284.6 eV suggesting the formation of $sp^2$ hybridized graphitic structure that can improve the electroconductivity of the samples, which is beneficial to fast electron transfer throughout the structural frameworks.[27] In addition, the C 1s can be further deconvoluted into peaks positioned at 284.8, 285.8, and 288.8 eV, which may attribute to C=C, C=N/C-O/C-S, and C-N, respectively.[55, 64-66] Combining XPS analysis with XRD results, it is believed that the products derived from the sulfurization of ZIF-67 at high temperature are basically $Co_xS_y$ supported on N,S-codoped carbon composites.

The textural characteristics of the as-synthesised composites were analysed by $N_2$ sorption at -196 °C. While sample $Co_xS_y$@C-600 exhibits a large hysteresis loop between its adsorption and desorption branches, implying the existence of mesoporous feature due to the voids between particles, the other two samples $Co_xS_y$@C-800, and $Co_xS_y$@C-1000 show largely reversible adsorption–desorption isotherms. These 3 samples exhibited specific surface area of 178, 238, and 248 $m^2$ $g^{-1}$ and pore volume of 0.80, 0.35, and 0.31 $cm^3$ $g^{-1}$, respectively (shown in Table S1), much lower than that of the ZIF-67 precursor (shown in Fig. 4 and Fig. S1c†), probably

to the dominance of cobalt sulfide weight percentage in the as-synthesised composites. The relative large surface area of the composites is beneficial to provide more accessible active sites, which is likely to result in a higher electrocatalytic activity.[39]

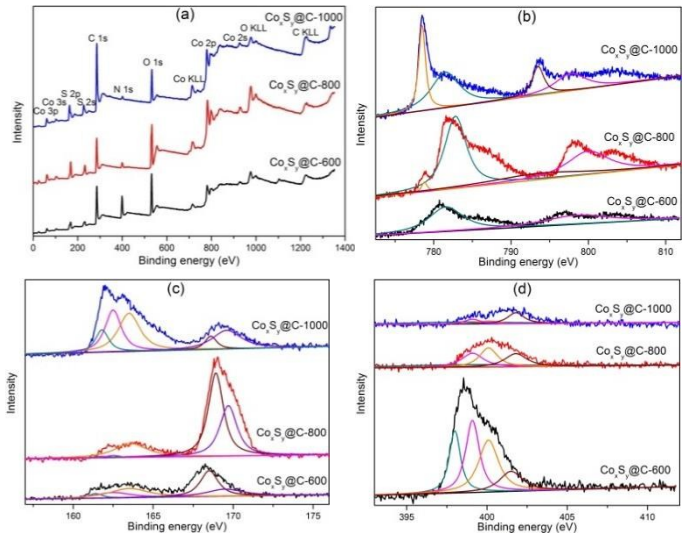


**Fig. 3 (a) Element survey by XPS and high-resolution XPS spectrum of (b) Co 2p, (c) S 2p and (d) N 1s for the as-synthesised $Co_xS_y$@C composites.**

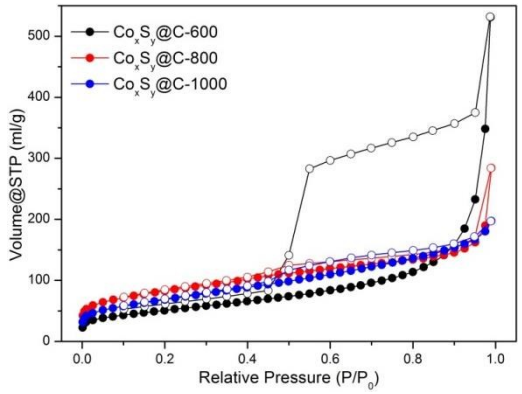


**Fig. 4 Nitrogen adsorption-desorption isotherm curves of the as-synthesised $Co_xS_y$@C composites.**

The thermal stabilities of the composites in air were evaluated by TGA-MS. As shown in the TGA profiles (Fig. S6a†), all the as-synthesised composites exhibit a minor weight loss event below 100 °C due to the removal of adsorbed water from the composites (Fig. S6c†), followed by a small weight increase in the temperature range of 300-500 °C, due to the oxidation of cobalt sulfide to high valence state. There are then two major weight loss events at 450-500 and 790 °C for all the samples, corresponding to the burn off the N,S-codoped carbon species in air, as confirmed by the emission of $CO_2$, $NO_2$ and $SO_2$ in their MS signals (see Fig. S6b, d and e†), and the decomposition and oxidation of cobalt sulfides (Fig. S6e†). It is worth noting that the sample $Co_xS_y$@C-600 shows different weight loss event in the temperature range of 300 - 500 °C, accompanying the evolving $CO_2$, $NO_2$ and $SO_2$ (see Fig. S6b, d and e†), maybe due to the oxidation of incomplete decomposition of organic ligands from the precursors.

The electrocatalytic activities of the as-prepared composites towards ORR are then evaluated by cyclic voltammetry (CV) measurements in 0.1 M KOH at 25 °C. Comparing the CV curves in $O_2$-versus $N_2$-saturated electrolyte solution, it clearly reveals that the composites are electrocatalytic active in ORR (Fig. 5a and Fig. S7†). As shown in Fig. 5a, no obvious redox peak is observed for $Co_xS_y$@C-1000 in $N_2$-saturated solution. In contrast, when the electrolyte is saturated with $O_2$, a well-defined cathodic peak clearly appears at -0.162 V, confirming the electrocatalytic activity for ORR.[67, 68] Other samples $Co_xS_y$@C-600 and $Co_xS_y$@C-800 (Fig. S7†) show a cathodic peak at -0.425 and -0.156 V, respectively. Noticeably, the sample $Co_xS_y$@C-1000 shows a much higher peak current (2.94 mA cm$^{-2}$) than those of $Co_xS_y$@C-600 (0.73 mA cm$^{-2}$) and $Co_xS_y$@C-800 (1.48 mA cm$^{-2}$), implying the pronounced ORR catalytic activity for $Co_xS_y$@C-1000.

Rotating disk electrode (RDE) measurements were performed to gain further insight into the ORR kinetics of the $Co_xS_y$@C composites. As shown in the polarization curves at 1600 rpm in 0.1 M KOH (Fig. 5b), $Co_xS_y$@C-1000 obviously holds the highest onset potential (around -0.04 V) and largest cathodic current density (-4.6 mA cm$^{-2}$), indicating its superior activity. The onset potential for $Co_xS_y$@C-1000 is close to that of the benchmark Pt/C catalyst (-0.02 V) while the half-wave potentials of them are very close, suggesting that $Co_xS_y$@C-1000 is a promising alternative catalyst for the cathodic ORR. In addition, the polarization curve of $Co_xS_y$@C-1000 is significantly different from that of $Co_xS_y$@C-600 and $Co_xS_y$@C-800 but resembles that of Pt/C, indicating that the ORR mechanism of $Co_xS_y$@C-1000 is different from those of the other $Co_xS_y$@C composites but is more like that of Pt/C, which exhibited an efficient four-electron ORR pathway.[69, 70] The mechanism of four-electron ORR pathway proceeds through two-oxygen atom side and/or bridge adsorption for oxygen dissociation simultaneously.[70]

RDE measurements at different rotating speeds were carried out and the kinetic parameters were analysed with the Koutecky-Levich (K-L) equation. An increase in the rotation speed leads to an increase in the diffusion of oxygen at the surface of the electrode, which results in large current densities as shown in Fig. 5c. The good linearity and near parallelism properties of K-L plots for $Co_xS_y$@C-1000 indicate first-order reaction kinetics with regard to the concentration of dissolved oxygen and similar electron transfer numbers (n) for ORR at various potentials (Fig. 5d).[71]

The value of *n* and kinetic current density ($J_k$) can be respectively derived from the slope and intercept of the K-L plots (Fig. 5d and Fig. S8†) at various potentials,[72] and the results are depicted in Fig. 5e. Obviously, the values of *n* for $Co_xS_y$@C-1000 varied from 3.69 to 3.78 in the potential range of -0.65 – -0.35V, suggesting that the ORR proceeded mainly through a four-electron pathway. This was further confirmed by the low $HO_2^-$ yield (~12%) and high *n* value (> 3.7) measured by the RRDE tests as shown in Fig. S9c and 9d. The mechan

of the four-electron transfer for ORR has been suggested to proceed through simultaneous two-oxygen atom side and/or bridge adsorption for oxygen dissociation.[70] In contrast, the *n* values for the other two composites decreased with the sulfurization temperature, and they are only 2.13-3.28 for the $Co_xS_y$@C-600, indicating that a two-electron pathway might dominate the $Co_xS_y$@C-600 catalysed ORR process. Moreover, the $J_k$ values for $Co_xS_y$@C-1000 were always much higher than those for the other two composites, reflecting the enhanced electron transfer kinetics of oxygen reduction. Compared with other different previously reported catalysts (shown in Table S2), the ORR catalytic performance of $Co_xS_y$@C-1000 is competitive.

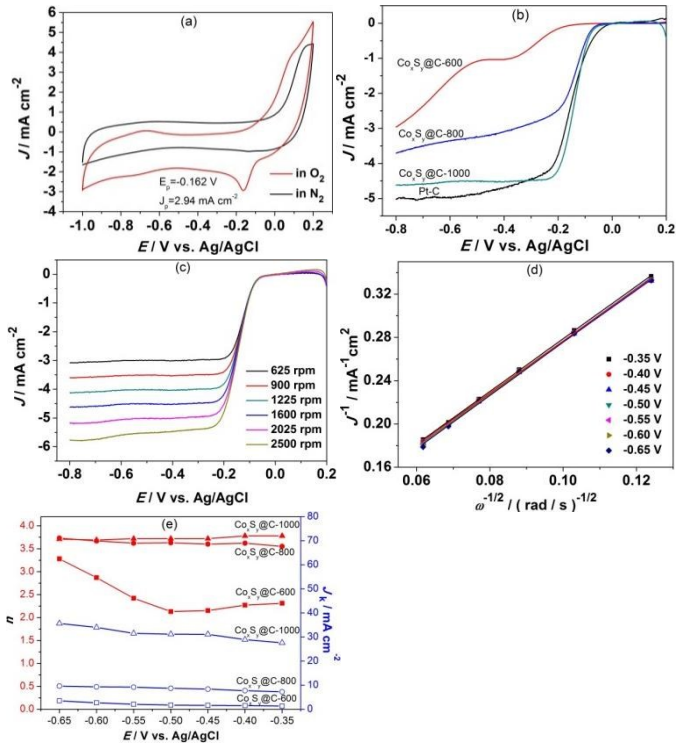


**Fig. 5 (a) CV curves of $Co_xS_y$@C-1000 composite in $N_2$- or $O_2$-saturated 0.1 M KOH. (b) ORR polarization curves of $Co_xS_y$@C-600, $Co_xS_y$@C-800, $Co_xS_y$@C-1000, and Pt/C at 1600 rpm. (c) ORR polarization curves of $Co_xS_y$@C-1000 at different rotating speeds. (d) K-L plots of $Co_xS_y$@C-1000 at different potentials. (e) Electron transfer numbers (n) and the corresponding kinetic current density ($J_k$) of $Co_xS_y$@C-600, $Co_xS_y$@C-800, and $Co_xS_y$@C-1000 as a function of the electrode potentials.**

The superior ORR activity of the $Co_xS_y$@C-based composites is attributed to their novel structures. The pristine cobalt sulfides have major drawbacks in capacity fading and low conductivity. To overcome these obstacles, the cobalt sulfide nanoparticles can uniformly disperse into the heteroatom-doped carbon matrix, which formed a conducting network to the electrode and facilitate ORR through effective charge transport between oxygen molecules adsorbed on cobalt sulfide active sites and the electrode. The utilisation of molecular-like porous ZIF-67 as precursor not only enable the generated cobalt sulfide nanoparticles homogeneously dispersed on porous carbon matrix, but also the porous carbons can serve as a substrate and good conductor t provide more accessible cobalt sulfide active site consequently further enhancement of the ORR activity can b realised. Specifically, for sample $Co_xS_y$@C-1000, the core-shell structure between the active cobalt sulfide nanoparticles an the porous carbon shells provides superior facile pathways for electron and mass transport.[43] In addition, heteroatom dope (N and S-doped) carbon also plays an important role in the ORR activity enhancement. By modifying the electronic an geometric properties of carbon matrix, N and S doping can no only provide more active sites, but also enhance the interaction between carbon structure and active catalyti sites.[27] The defects in carbon caused by N and S doping ca result in much stronger adsorption of oxygen molecules an the higher activity for heterogeneous peroxid decomposition.[27]

Besides the catalytic activities, the durability of $Co_xS_y$@C-1000 composites and commercial Pt/C was tested at -0.15 V in 0.1 M KOH over 18000 s. It is observed that sample $Co_xS_y$@C-1000 is more durable than commercial Pt/C (see Fig. 6a). The relative current of the sample $Co_xS_y$@C-10 which was measured by chronoamperometry at a consta potential of -0.15 V after 18000 s, is 92%, but for Pt/C th value is only 74%. Such a high durability of $Co_xS_y$@C-100 composite is due to the presence of the porous carbon matri which provides a conducting substrate and good electrochemical coupling between the substrate and oxyge molecules, and thus facilitates the ORR through the effective transportation of electrons between the oxygen molecules an the active sites of electrode. Moreover, the N and S co-doping on porous carbon shell may also play a role to form muc stronger adsorption of oxygen molecules and the higher activity for heterogeneous peroxide decomposition. I addition, the unique core-shell structure of $Co_xS_y$@C-1000 composites also offers a better conducting substrate a excellent electrochemical coupling between the substrate and oxygen molecules.

Methanol crossover is one of the major disadvantages fo Pt/C catalyst in ORR.[23, 73] Thus, 1 M methanol was added int the 0.1 M KOH electrolyte solution to investigate the metha tolerance for the as-synthesised composites under the sam conditions as Pt/C. The results (see Fig. 6b) show that th introduction of methanol causes a sharp decrease in th current density for the Pt/C catalyst. In contrast, methanol ha negligible effect on the performance of $Co_xS_y$@C-100 composite at the cathode. The high durability and remarkabl methanol tolerance give $Co_xS_y$@C-1000 superiority over th commercial Pt/C and thus it is a promising electrocatalyst fo the cathodic ORR.

Excitingly, besides the high ORR activities, the $Co_xS_y$@ composites also exhibit excellent electrocatalytic performances in OER (Fig. 7). Obviously, Pt/C is not a goo catalyst for OER and much higher overpotential is required to achieve the current density of 10 mA $cm^{-2}$. Compared with sample $Co_xS_y$@C-600, $Co_xS_y$@C-800 and Pt/C, the higher

current density and an earlier onset of catalytic current are observed for sample $Co_xS_y$@C-1000, indicating that $Co_xS_y$@C-1000 is a highly active OER catalyst. As shown in Fig. 7a, an anodic peak of $Co_xS_y$@C-1000 is seen at around 0.3 V preceding the oxygen evolution, which can be attributed to the fact that cobalt sulfide nanoparticles in $Co_xS_y$@C-1000 are partly oxidized into cobalt oxide, forming the cobalt oxide/cobalt sulfide complex species.[74] The current density of 10 mA $cm^{-2}$ can be achieved at a small overpotential of 0.47 V vs RHE for $Co_xS_y$@C-1000, much lower than that of $Co_xS_y$@C-800 (0.63 V vs RHE), but slightly higher than that of $IrO_2$ (0.45V vs RHE). It is believed that the introduction of cobalt sulfide and N, S dopants results in the adjacent carbon atoms positively charged, which can not only facilitate the adsorption

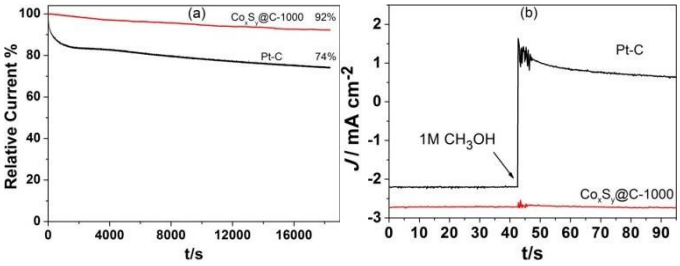


**Fig. 6 (a) Current–time chronoamperometric responses of $Co_xS_y$@C-1000 and Pt/C at -0.15 V in $O_2$-saturated 0.1 M KOH solution (1600 rpm). (b) Chronoamperometric responses of $Co_xS_y$@C-1000, and Pt/C at -0.15 V in $O_2$-saturated 0.1 M KOH solution (1600 rpm) with the addition of 1 M methanol.**

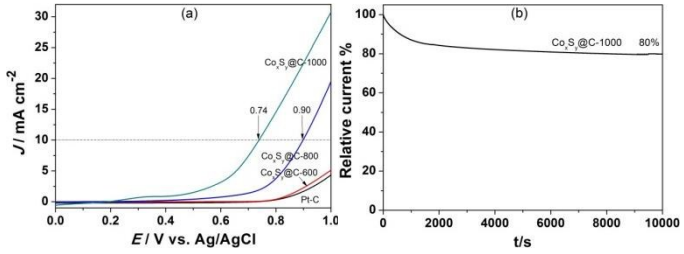


**Fig. 7 (a) Linear sweep voltammetry (LSV) polarization curves of $Co_xS_y$@C-600, $Co_xS_y$@C-800, $Co_xS_y$@C-1000, and Pt/C at 5 mV $s^{-1}$ in $N_2$-saturated 0.1 M KOH solution. (b) Chronoamperometric response for $Co_xS_y$@C-1000 at 0.8 V vs Ag/AgCl.**

of OH ions, but also promote the electron transfer between the catalyst surfaces and reaction intermediates.[75-77] Significantly, the potential acquired for the current density of 10 mA $cm^{-2}$ of $Co_xS_y$@C-1000 is comparable to those of other reported OER catalysts (as shown in Table S3). Furthermore, in the chronoamperometric test, the sample $Co_xS_y$@C-1000 can remain 80% its relative current after 10000 s (Fig. 7b), implying high durability of sample $Co_xS_y$@C-1000 in OER. Although oxidation may occur in Co-based OER catalyst,[78, 79] it is believed that the surface property of the cobalt sulfide can be still maintained during the OER stability test, even though the cobalt sulfide was partly oxidized.[24] In the case of the sample $Co_xS_y$@C-1000, we believe the composite was largely maintained during the OER stability test since the unique core-shell structures of the composites can protect the catalytic active cobalt sulfide from oxidation. It is likely that the a small amount of cobalt sulfide nanoparticles without carbon sh… protections may be partly oxidized in the process of OER at 0.8 V vs Ag/AgCl for 2000 s which cause the slightly decay of catalytic performance.

In our work, the whole system of the cobalt sulfide/porou… carbon materials is complicated as the as-synthesised composites containing different phases of cobalt sulfides, an… nitrogen, sulfur (with different contents) co-doped porous carbons, and even the structure of the composites can affec… the ORR and OER performance. Therefore, it is difficult to analyse each contribution of the materials separately. But it is believed that the higher electrocatalytic activity is led by the whole system.[45, 46] Clearly, the sample $Co_xS_y$-1000 shows th… best performance in ORR and OER. We believe that the mai… parameters that contribute to the higher electrocatalyti… activity may be due to the highly crystalized cobalt sulfide… combined with the synergistic effect between $Co_xS_y$ and … porous carbons, the N and S doping may play the auxiliary roles. Moreover, the protective porous carbon substrate (… catalytic active CoxSy) and the unique core-shell structure of CoxSy@C-1000 may contribute to the excell… electrochemical stability.

Considering the easiness of preparation of $Co_xS_y$@C-1000 via a simple one-step sulfurization and carbonization of zeolit… imidazolate frameworks simultaneously, its cost-effective an… much cheaper than the benchmarked Pt/C catalyst,[39] the remarkable features of excellent activities, favourable kinetic… and high electrochemical stabilities, the current $Co_xS_y$@C-1000 sample may be one of the most promising alternativ… bifunctional electrocatalysts in both ORR and OER.

## Conclusions

In summary, using ZIF-67 as a precursor, a facile one-step sulfurization and carbonization route has been successfu… developed to synthesise atomically uniform dispersed cobalt sulfide nanocrystal particles embedded in N, S-codoped porous carbon matrices, which are promising advanced bifunctiona… electrocatalyst for ORR and OER. Due to the high porosity, unique core-shell structure, homogeneous dispersion and … and S-doping effect, the as-synthesised nanocomposit… $Co_xS_y$@C-1000 not only exhibits exceptionally prominen… electrocatalytic activity, good methanol tolerance and superio… durability for ORR, but also offers promising catalytic performance for OER in alkaline medium. This work may ope… up a new avenue for the design and syntheses of highly homogeneous dispersed porous carbon-metal sulfide nanocomposite materials that display low-cost and efficien… bifunctional electrocatalytic behaviours for the nex… generation of energy conversion and storage applications.

## Acknowledgements

The financial support by the Royal Society, the Royal Academy of Engineering and University of Exeter is greatly acknowledged.

## References

1. S. Chu and A. Majumdar, *Nature*, 2012, **488**, 294-303.
2. I. Katsounaros, S. Cherevko, A. R. Zeradjanin and K. J. J. Mayrhofer, *Angew. Chem. Int. Ed.*, 2014, **53**, 102-121.
3. C. Yuan, H. B. Wu, Y. Xie and X. W. Lou, *Angew. Chem. Int. Ed.*, 2014, **53**, 1488-1504.
4. B. C. H. Steele and A. Heinzel, *Nature*, 2001, **414**, 345-352.
5. H. A. Gasteiger and N. M. Marković, *Science*, 2009, **324**, 48-49.
6. G. Wu and P. Zelenay, *Acc. Chem. Res.*, 2013, **46**, 1878-1889.
7. S. Xie, S.-I. Choi, N. Lu, L. T. Roling, J. A. Herron, L. Zhang, J. Park, J. Wang, M. J. Kim, Z. Xie, M. Mavrikakis and Y. Xia, *Nano Lett.*, 2014, **14**, 3570-3576.
8. K. A. Kuttiyiel, K. Sasaki, Y. Choi, D. Su, P. Liu and R. R. Adzic, *Nano Lett.*, 2012, **12**, 6266-6271.
9. D. J. Li, U. N. Maiti, J. Lim, D. S. Choi, W. J. Lee, Y. Oh, G. Y. Lee and S. O. Kim, *Nano Lett.*, 2014, **14**, 1228-1233.
10. H. Wang and H. Dai, *Chem. Soc. Rev.*, 2013, **42**, 3088-3113.
11. L. Dai, Y. Xue, L. Qu, H.-J. Choi and J.-B. Baek, *Chemical Reviews*, 2015, **115**, 4823-4892.
12. S.-L. Li and Q. Xu, *Energy Environ. Sci.*, 2013, **6**, 1656-1683.
13. J. Zhang, Z. Zhao, Z. Xia and L. Dai, *Nat Nano*, 2015, **10**, 444-452.
14. Y. Liang, Y. Li, H. Wang, J. Zhou, J. Wang, T. Regier and H. Dai, *Nat Mater*, 2011, **10**, 780-786.
15. H. A. Gasteiger, S. S. Kocha, B. Sompalli and F. T. Wagner, *Appl. Catal., B*, 2005, **56**, 9-35.
16. M. Lefèvre, E. Proietti, F. Jaouen and J.-P. Dodelet, *Science*, 2009, **324**, 71-74.
17. J. Duan, S. Chen, S. Dai and S. Z. Qiao, *Adv. Funct. Mater.*, 2014, **24**, 2072-2078.
18. H. Wang, Y. Liang, Y. Li and H. Dai, *Angew. Chem. Int. Ed.*, 2011, **50**, 10969-10972.
19. N. A. Vante and H. Tributsch, *Nature*, 1986, **323**, 431-432.
20. R. A. Sidik and A. B. Anderson, *J. Phys. Chem. B*, 2006, **110**, 936-941.
21. Y.-X. Zhou, H.-B. Yao, Y. Wang, H.-L. Liu, M.-R. Gao, P.-K. Shen and S.-H. Yu, *Chem. Eur. J.*, 2010, **16**, 12000-12007.
22. Y. Feng, T. He and N. Alonso-Vante, *Chem. Mater.*, 2008, **20**, 26-28.
23. M.-R. Gao, Q. Gao, J. Jiang, C.-H. Cui, W.-T. Yao and S.-H. Yu, *Angew. Chem. Int. Ed.*, 2011, **50**, 4905-4908.
24. P. Ganesan, M. Prabu, J. Sanetuntikul and S. Shanmugam, *ACS Catalysis*, 2015, **5**, 3625-3637.
25. N. Mahmood, C. Zhang, J. Jiang, F. Liu and Y. Hou, *Chem. Eur. J.*, 2013, **19**, 5183-5190.
26. Q. Liu and J. Zhang, *CrystEngComm*, 2013, **15**, 5087-5092.
27. Q. Li, R. Cao, J. Cho and G. Wu, *Adv. Energy Mater.*, 2014, **4**, n/a-n/a.
28. Y. Zhao, R. Nakamura, K. Kamiya, S. Nakanishi and K. Hashimoto, *Nat Commun*, 2013, **4**.
29. R. Silva, D. Voiry, M. Chhowalla and T. Asefa, *J. Am. Chem. Soc.*, 2013, **135**, 7823-7826.
30. K. Gong, F. Du, Z. Xia, M. Durstock and L. Dai, *Science*, 2009, **323**, 760-764.
31. B. Chen, Z. Yang, Y. Zhu and Y. Xia, *J. Mater. Chem. A*, 2014, **2**, 16811-16831.
32. B. Wang, A. P. Cote, H. Furukawa, M. O/'Keeffe and O. M. Yaghi, *Nature*, 2008, **453**, 207-211.
33. A. Phan, C. J. Doonan, F. J. Uribe-Romo, C. B. Knobler, M. O'Keeffe and O. M. Yaghi, *Acc. Chem. Res.*, 2010, **43**, 58-67.
34. W. Xia, J. Zhu, W. Guo, L. An, D. Xia and R. Zou, *J. Mater. Chem. A*, 2014, **2**, 11606-11613.
35. X. Wang, J. Zhou, H. Fu, W. Li, X. Fan, G. Xin, J. Zheng and X. Li, *J. Mater. Chem. A*, 2014, **2**, 14064-14070.
36. N. L. Torad, R. R. Salunkhe, Y. Li, H. Hamoudi, M. Imura, Y. Sakka, C.-C. Hu and Y. Yamauchi, *Chem. Eur. J.*, 2014, **20**, 7895-7900.
37. W. Chaikittisilp, N. L. Torad, C. Li, M. Imura, N. Suzuki, S. Ishihara, K. Ariga and Y. Yamauchi, *Chem. Eur. J.*, 2014, **20**, 4217-4221.
38. N. L. Torad, M. Hu, S. Ishihara, H. Sukegawa, A. A. Belik, M. Imura, K. Ariga, Y. Sakka and Y. Yamauchi, *Small*, 2014, **10**, 2096-2107.
39. Y. Hou, Z. Wen, S. Cui, S. Ci, S. Mao and J. Chen, *Adv. Funct. Mater.*, 2015, **25**, 872-882.
40. Z. Jiang, H. Sun, Z. Qin, X. Jiao and D. Chen, *Chem Commun (Camb)*, 2012, **48**, 3620-3622.
41. Z. Jiang, W. Lu, Z. Li, K. H. Ho, X. Li, X. Jiao and D. Chen, *J. Mater. Chem. A*, 2014, **2**, 8603-8606.
42. J. Qian, F. Sun and L. Qin, *Mater. Lett.*, 2012, **82**, 220-223.
43. M. Shen, C. Ruan, Y. Chen, C. Jiang, K. Ai and L. Lu, *ACS Appl. Mater. Interfaces*, 2014, **7**, 1207-1218.
44. F. Bai, Y. Xia, B. Chen, H. Su and Y. Zhu, *Carbon*, 2014, **79**, 213-226.
45. R. Wu, D. P. Wang, X. Rui, B. Liu, K. Zhou, A. W. K. Law, Q. Yan, J. Wei and Z. Chen, *Adv. Mater.*, 2015, **27**, 3038-3044.
46. Q. Wang, R. Zou, W. Xia, J. Ma, B. Qiu, A. Mahmood, R. Zhao, Y. Yang, D. Xia and Q. Xu, *Small*, 2015, **11**, 2511-2517.
47. A. C. Ferrari, *Solid State Commun.*, 2007, **143**, 47-57.
48. C. Castiglioni, F. Negri, M. Rigolio and G. Zerbi, *J. Chem. Phys.*, 2001, **115**, 3769-3778.
49. C. N. R. Rao and K. P. R. Pisharody, *Prog. Solid State Chem.*, 1976, **10, Part 4**, 207-270.
50. L. Lai, J. R. Potts, D. Zhan, L. Wang, C. K. Poh, C. Tang, H. Gong, Z. Shen, J. Lin and R. S. Ruoff, *Energy Environ. Sci.*, 2012, **5**, 7936-7942.
51. S.-J. Bao, Y. Li, C. M. Li, Q. Bao, Q. Lu and J. Guo, *Cryst. Growth Des.*, 2008, **8**, 3745-3749.
52. J. F. Marco, J. R. Gancedo, M. Gracia, J. L. Gautier, E. I. Rios, H. M. Palmer, C. Greaves and F. J. Berry, *J. Mater. Chem.*, 2001, **11**, 3087-3093.
53. Q. Liu, J. Jin and J. Zhang, *ACS Appl. Mater. Interfaces*, 2013, **5**, 5002-5008.
54. X. Wang, Q. Xiang, B. Liu, L. Wang, T. Luo, D. Chen and G. Shen, *Sci. Rep.*, 2013, **3**.
55. S.-A. Wohlgemuth, R. J. White, M.-G. Willinger, M.-M. Titirici and M. Antonietti, *Green Chem.*, 2012, **14**, 1515-1523.
56. Z. Yang, Z. Yao, G. Li, G. Fang, H. Nie, Z. Liu, X. Zhou, X. A. Chen and S. Huang, *ACS Nano*, 2012, **6**, 205-211.
57. K. Polychronopoulou, C. D. Malliakas, J. He and M. G. Kanatzidis, *Chem. Mater.*, 2012, **24**, 3380-3392.
58. V. N. Bui, D. Laurenti, P. Delichère and C. Geantet, *Appl. Catal., B*, 2011, **101**, 246-255.
59. H. S. Kim, T. S. Arthur, G. D. Allred, J. Zajicek, J. G. Newman, A. E. Rodnyansky, A. G. Oliver, W. C. Boggess and J. Muldoon, *Nat Commun*, 2011, **2**, 427.



 

60. S. Das, P. Sudhagar, S. Nagarajan, E. Ito, S. Y. Lee, Y. S. Kang and W. Choi, *Carbon*, 2012, **50**, 4815-4821.
61. G. Wang, J. Zhang, S. Kuang, S. Liu and S. Zhuo, *J. Power Sources*, 2014, **269**, 473-478.
62. Z.-S. Wu, L. Chen, J. Liu, K. Parvez, H. Liang, J. Shu, H. Sachdev, R. Graf, X. Feng and K. Müllen, *Adv. Mater.*, 2014, **26**, 1450-1455.
63. X. Zou, X. Huang, A. Goswami, R. Silva, B. R. Sathe, E. Mikmeková and T. Asefa, *Angew. Chem.*, 2014, **126**, 4461-4465.
64. Y. Dong, H. Pang, H. B. Yang, C. Guo, J. Shao, Y. Chi, C. M. Li and T. Yu, *Angew. Chem. Int. Ed.*, 2013, **52**, 7800-7804.
65. S. Yang, L. Zhi, K. Tang, X. Feng, J. Maier and K. Müllen, *Adv. Funct. Mater.*, 2012, **22**, 3634-3640.
66. J. Wang, H.-x. Zhong, Y.-l. Qin and X.-b. Zhang, *Angew. Chem. Int. Ed.*, 2013, **52**, 5248-5253.
67. S. Chen, Z. Wei, X. Qi, L. Dong, Y.-G. Guo, L. Wan, Z. Shao and L. Li, *J. Am. Chem. Soc.*, 2012, **134**, 13252-13255.
68. D.-S. Yang, D. Bhattacharjya, S. Inamdar, J. Park and J.-S. Yu, *J. Am. Chem. Soc.*, 2012, **134**, 16127-16130.
69. Y. Zheng, Y. Jiao, L. Ge, M. Jaroniec and S. Z. Qiao, *Angew. Chem. Int. Ed.*, 2013, **52**, 3110-3116.
70. S. Kattel, P. Atanassov and B. Kiefer, *Phys. Chem. Chem. Phys.*, 2013, **15**, 148-153.
71. Y. Li, W. Zhou, H. Wang, L. Xie, Y. Liang, F. Wei, J.-C. Idrobo, S. J. Pennycook and H. Dai, *Nat Nano*, 2012, **7**, 394-400.
72. K. J. J. Mayrhofer, D. Strmcnik, B. B. Blizanac, V. Stamenkovic, M. Arenz and N. M. Markovic, *Electrochim. Acta*, 2008, **53**, 3181-3188.
73. C. Zhang, R. Hao, H. Yin, F. Liu and Y. Hou, *Nanoscale*, 2012, **4**, 7326-7329.
74. S. Mao, Z. Wen, T. Huang, Y. Hou and J. Chen, *Energy Environ. Sci.*, 2014, **7**, 609-616.
75. S. Chen, J. Duan, J. Ran, M. Jaroniec and S. Z. Qiao, *Energy Environ. Sci.*, 2013, **6**, 3693-3699.
76. J. Masa, W. Xia, I. Sinev, A. Zhao, Z. Sun, S. Grützke, P. Weide, M. Muhler and W. Schuhmann, *Angew. Chem. Int. Ed.*, 2014, **53**, 8508-8512.
77. M. Li, L. Zhang, Q. Xu, J. Niu and Z. Xia, *J. Catal.*, 2014, **314**, 66-72.
78. H. S. Ahn and T. D. Tilley, *Adv. Funct. Mater.*, 2013, **23**, 227-233.
79. L. Trotochaud, J. K. Ranney, K. N. Williams and S. W. Boettcher, *J. Am. Chem. Soc.*, 2012, **134**, 17253-17261.